Long-time simulations of the Kelvin-Helmholtz instability using an adaptive vortex method

Sung-Ik Sohn
Department of Mathematics, Kangnung-Wonju National University, Kangnung 210-702, South Korea

Daeki Yoon
Department of Mathematics, Korea University, Seoul 130-701, South Korea

Woonjae Hwang
Department of Information and Mathematics, Korea University, Jochiwon 339-700, South Korea

(Received 12 July 2010; published 26 October 2010)

The nonlinear evolution of an interface subject to a parallel shear flow is studied by the vortex sheet model. We perform long-time computations for the vortex sheet in density-stratified fluids by using the point vortex method and investigate late-time dynamics of the Kelvin-Helmholtz instability. We apply an adaptive point insertion procedure and a high-order shock-capturing scheme to the vortex method to handle the nonuniform distribution of point vortices and enhance the resolution. Our adaptive vortex method successfully simulates chaotically distorted interfaces of the Kelvin-Helmholtz instability with fine resolutions. The numerical results show that the Kelvin-Helmholtz instability evolves a secondary instability at a late time, distorting the internal rollup, and eventually develops to a disordered structure.

DOI: 10.1103/PhysRevE.82.046711 PACS number(s): 02.70.Pt, 47.20.Ft, 47.32.C−

I. INTRODUCTION

A perturbed interface between fluids subject to a parallel shear flow is unstable. This interfacial instability is known as Kelvin-Helmholtz (KH) instability and is one of classical problems in fluid dynamics [1,2]. A linear stability analysis dates back to the 19th century, and computations of the nonlinear formation of the rollup of the interface are among earliest examples of computational fluid dynamics [1]. The linear and early nonlinear stages of the KH instability are well understood, but late-time dynamics, where the interface is chaotically disordered and the rollup has a complex internal structure, is less discovered. The understanding of late-time dynamics of the KH instability is important not only in its own interests, but also in the study of turbulence and mixing, where the KH instability plays a dominant role [3,4].

A vortex sheet is a simple model for the interface of a parallel shear flow, and the vortex method is the numerical method based on the vortex sheet model [1,5]. In this model, the interface is approximated by a surface across which the tangential velocity is discontinuous. The vortex sheet model has an elegant formulation, but turned out to be not convenient for computations due to the formation of the singularity [1,6]. Moore [6] showed that a singularity forms in the vortex sheet at a finite time. The difficulty of the vortex method was resolved by a regularization of the integral kernel in the model [7].

In this paper, we present long-time computations for the KH instability of finite density contrast by using the vortex method. In the vortex method, the interface is considered as a set of point vortices, and these vortices are computed in a Lagrangian manner, not solving equations in whole two-dimensional grids. This advantage of the vortex method provides accurate solutions for the evolution of unstable interfaces.

The numerical simulations of the KH instability by the vortex method have been performed by many people [7–13]. However, most of previous simulations were limited to the vortex sheet in a uniform density fluid. Several authors [8,13] conducted the computations for the KH instability in density-stratified fluids, but the results were given only for early stages of the rollup. To the authors' knowledge, results for the highly distorted KH interface at a late time were obtained only for a uniform density case [11,12]. The purpose of this paper is the long-time simulations for the vortex sheet of finite density contrast and the investigation of late-time dynamics for the KH instability.

A main difficulty in the long-time computations of the vortex sheet is the lack of resolution resulting from the nonuniform distribution of point vortices. At an early stage of the interface evolution, the point vortices tend to cluster around a vortex core and diverge at the outside region. However, at late times, point clustering and diverging occur irregularly along the interface, which makes the interface poorly resolved. The simulation with many vortices initially is a naive way to enhance the resolution, but for long-time simulations it is very expensive and usually beyond the computing capability, since the computation cost of the vortex method at each time step is $O(N^2)$, where N is the number of vortices.

To overcome the nonuniform distribution of point vortices, we apply a point insertion procedure which adaptively adds the vortices to the region of low resolution. Our point insertion method is an extension of the method presented by Krasny [14] for the uniform fluid to the density-stratified fluids. In the case of density stratification, the point insertion is not an easy task, because the governing equations for the vortex method are coupled, and variables of a previous time step are also needed in the insertion procedure.

A redistribution procedure, which relocates the vortices on the interface uniformly in the arclength or a parameter, is another way to handle the nonuniform distribution of point vortices. However, the redistribution algorithm should be devised with high accuracy and applied carefully, because it

may involve the numerical diffusion. Note that Rangel and Sirignano [8] used the redistribution procedure and yielded the excessive smoothing on the solution. Kerr [15] presented a systematic redistribution procedure for the vortex sheet in stratified fluids. The redistribution procedure by Kerr has a predictor and corrector step to shift the point vortices, and thus is rather complicated.

Besides the nonuniform distribution of point vortices, a difficulty also lies in the computation of the vortex sheet strength. In density-stratified fluids, the equation for the vortex sheet strength is coupled with the governing dynamical equation, and the accurate calculation of the vortex sheet strength is critically important in the vortex method. In the KH-type instability, the profile of the vortex sheet strength becomes very steep and eventually evolves shocks and peaks along the interface.

A shock-capturing method, which has been well developed for hyperbolic conservation laws [16], can be adopted for the stable computation of the vortex sheet strength. Previously the Godunov method was employed to the computation of the vortex sheet strength [13,17]. However, the Godunov method is only first-order accurate and smoothes the shocks and peaks of the profile, which may result a significant change in the evolution of the interface at a late time. The adoption of a high-order shock-capturing method to the vortex method is needed for the long-time computation, but a difficulty is that the point vortices are located nonuniformly, and most of shock-capturing methods are developed for the uniform grid.

We apply the weighted essentially nonoscillating (WENO) scheme [18–20] for the high-order computation of the vortex sheet strength. The WENO scheme has been widely used in the hyperbolic conservation laws. The WENO scheme gives a high resolution around the peak and shock without spurious oscillations and is capable to implement a type of problems of nonuniform grids, within the original framework of the methodology. This couple of advantages of the WENO scheme is found to be appropriate for the vortex method.

The paper is organized as follows. Section II gives the description of the vortex sheet model in density-stratified fluids, and Sec. III describes the adaptive numerical method for the vortex model. The computational results are presented in Sec. IV. Section V gives the conclusion.

II. VORTEX SHEET MODEL

In this section we briefly present the vortex sheet model in density-stratified fluids. The full derivation of the model is referred to Tryggvason [21].

We consider an interface separating two fluids of different densities in two dimensions. The fluids are inviscid, incompressible, and irrotational, and the motion of fluids is governed by the Euler equation

$$\mathbf{a}_i = -\frac{1}{\rho_i}\nabla p_i, \quad i=1,2, \tag{1}$$

where $\mathbf{a}$ is the acceleration of a fluid particle, ρ is the density of the fluid, and p is the pressure in the fluid. From the potential flow assumption, the interface can be modeled as a vortex sheet. The strength of the vortex sheet γ is defined as the jump in the tangential velocities of two fluids across the interface,

$$\gamma = (\mathbf{u}_1 - \mathbf{u}_2)\cdot\mathbf{s}. \tag{2}$$

Here, $\mathbf{u}_1$ and $\mathbf{u}_2$ are the velocities above and below the interface, respectively, and $\mathbf{s}$ is the unit tangent vector at the interface.

The Lagrangian velocity of the interface is expressed by

$$\mathbf{q} = \mathbf{U} + \tfrac{1}{2}\gamma\alpha\mathbf{s}, \tag{3}$$

where $\mathbf{U}$ represents the average of the velocity on either side,

$$\mathbf{U} = \tfrac{1}{2}(\mathbf{u}_1 + \mathbf{u}_2), \tag{4}$$

and α ($|\alpha|\le 1$) is the weighting parameter. Taking $\alpha=1$, the vortices follow the upper fluid and, taking $\alpha=-1$, the vortices follow the lower fluid. In all our computations, α is set to zero.

The interface is described by a parametric curve $\mathbf{x}=\mathbf{x}(s,t)=[x(s,t),y(s,t)]$, with the arclength s and time t, and is evolved by

$$\frac{d\mathbf{x}}{dt} = \mathbf{q}. \tag{5}$$

The average velocity $\mathbf{U}=(u,v)$ is determined by the Birkhoff-Rott equation [1]. For the periodic boundary condition with a period λ, the Birkhoff-Rott equation is of the form

$$u - iv = \frac{i}{2\lambda}\int_0^\lambda \tilde{\gamma}\cot\frac{\pi(z-\tilde{z})}{\lambda}d\tilde{s}. \tag{6}$$

Here, $z=x+iy$ in complex notation, and $\tilde{\gamma}=\gamma(\tilde{s})$, $z=z(s)$, and $\tilde{z}=z(\tilde{s})$.

To obtain the average velocity by Eq. (6), the evolution equation for the vortex sheet strength γ is needed. The acceleration $\mathbf{a}_i$ at the interface has the following kinematic relation:

$$\mathbf{a}_i = \frac{d\mathbf{u}_i}{dt} - \frac{1}{2}\gamma(\alpha \pm 1)\frac{\partial \mathbf{u}_i}{\partial s}, \tag{7}$$

where the + (−) sign is for $i=2$ (1). Subtracting the tangential component of the Euler equation (1) of each fluid and using Eq. (7), we have

$$\begin{aligned}(\mathbf{a}_1 - \mathbf{a}_2)\cdot\mathbf{s} &= A(\mathbf{a}_1 + \mathbf{a}_2)\cdot\mathbf{s} \\ &= A\left(2\frac{d\mathbf{U}}{dt}\cdot\mathbf{s} + \frac{1}{4}\frac{\partial\gamma^2}{\partial s} - \gamma\alpha\frac{\partial\mathbf{U}}{\partial s}\cdot\mathbf{s}\right),\end{aligned} \tag{8}$$

where $A=(\rho_2-\rho_1)/(\rho_2+\rho_1)$ is the Atwood number. Then, by relation (7), Eq. (8) becomes

$$\frac{d\gamma}{dt} = 2A\frac{d\mathbf{U}}{dt}\cdot\mathbf{s} + \frac{\alpha+A}{4}\frac{\partial\gamma^2}{\partial s} - (1+\alpha A)\gamma\frac{\partial\mathbf{U}}{\partial s}\cdot\mathbf{s}. \tag{9}$$

Equations (5), (6), and (9) give the evolution of the vortex sheet between stratified fluids. Note that Eq. (9) is actually

an integro-differential equation for γ since $\mathbf{U}$ is coupled to γ by Eq. (6).

III. NUMERICAL METHOD

A. Main algorithm

The Kelvin-Helmholtz instability develops a rollup due to the formation of a singularity, and this produces a difficulty in numerical computations. To overcome this, we apply a desingularization parameter $\delta>0$ to Eq. (6), following Krasny [7]. The "δ equations" for Eq. (6), assuming the period $\lambda=1$, are

$$u=\frac{1}{2}\int_0^1 \frac{\sinh 2\pi(y-\tilde{y})}{\cosh 2\pi(y-\tilde{y})-\cos 2\pi(x-\tilde{x})+\delta^2}\tilde{\gamma}d\tilde{s}, \quad (10)$$

$$v=-\frac{1}{2}\int_0^1 \frac{\sin 2\pi(x-\tilde{x})}{\cosh 2\pi(y-\tilde{y})-\cos 2\pi(x-\tilde{x})+\delta^2}\tilde{\gamma}d\tilde{s}. \quad (11)$$

To solve the system of equations numerically, we discretize the interface $\{\mathbf{x}_i\}_{i=0}^N$ and the vortex sheet strength $\{\gamma_i\}_{i=0}^N$. Given $\{\mathbf{x}_i\}$ and $\{\gamma_i\}$, the velocity field can be evaluated from Eqs. (3), (10), and (11). Applying direct summations for the integral, Eqs. (10) and (11) are approximated by

$$u_i=\frac{1}{2}\sum_{j\neq i}\Gamma_j\frac{\sinh 2\pi(y_i-y_j)}{\cosh 2\pi(y_i-y_j)-\cos 2\pi(x_i-x_j)+\delta^2}, \quad (12)$$

$$v_i=-\frac{1}{2}\sum_{j\neq i}\Gamma_j\frac{\sin 2\pi(x_i-x_j)}{\cosh 2\pi(y_i-y_j)-\cos 2\pi(x_i-x_j)+\delta^2}. \quad (13)$$

Here, Γ_i represents the local circulation, defined as

$$\Gamma_i=\gamma_i\delta s_i, \quad (14)$$

where $\delta s_i=\sqrt{(x_{i+1}-x_{i-1})^2+(y_{i+1}-y_{i-1})^2}/2$.

The interface position and vortex sheet strength in time are determined by Eqs. (5) and (9)–(11). For time integrations of these coupled equations, we apply an iteration method. The numerical procedure of time integrations are described as follows: assuming that the discrete position $\mathbf{x}_i^n$, the average velocity $\mathbf{U}_i^n$, and the vortex sheet strength γ_i^n are given at the current time step n, we first estimate $d\gamma_i^n/dt$ by Eq. (9) with $d\mathbf{U}_i^{n-1}/dt$ at the previous time step. Then, we update γ_i^{n+1} and advance the interface by Eq. (5) with Eq. (3) by suitable time stepping methods. Using the updated values for the interface position and vortex sheet strength, the velocity field at the next time step, $\mathbf{U}_i^{n+1}$, is evaluated from Eqs. (12) and (13). Then, we can compute the new estimate for $d\mathbf{U}_i^n/dt$ by the central difference with respect to time, i.e.,

$$\frac{d\mathbf{U}_i^n}{dt}=\frac{\mathbf{U}_i^{n+1}-\mathbf{U}_i^{n-1}}{2\Delta t}. \quad (15)$$

This procedure is repeated until the convergence of $d\mathbf{U}_i^n/dt$. Initially, $d\mathbf{U}_i^0/dt$ is updated by the forward difference, $d\mathbf{U}_i^0/dt=(\mathbf{U}_i^1-\mathbf{U}_i^0)/\Delta t$. Note that, for the integration of time stepping, the trapezoidal method is applied to Eq. (5) for the interface, using the updated velocity $\mathbf{U}_i^{n+1}$ during the iteration, and Euler's method to Eq. (9) for the vortex sheet strength.

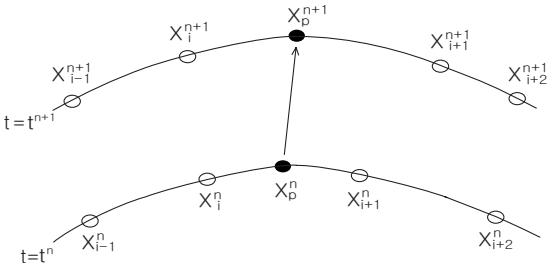

FIG. 1. Schematic of the point insertion. The distance of $\mathbf{x}_i^{n+1}$ and $\mathbf{x}_{i+1}^{n+1}$ exceeds a certain threshold, and to add a point between the two points, the point $\mathbf{x}_p^n$ is interpolated in the middle of $\mathbf{x}_i^n$ and $\mathbf{x}_{i+1}^n$ and is advanced by a time integration.

B. Point insertion procedure

At the end of each time step, we check each segment of the arclength, say Δs_i, and apply a point insertion procedure if Δs_i exceeds some threshold value Δs_{lim}. The point insertion procedure in density-stratified fluids is much more complicated than that in the uniform fluid, because the model has two coupled equations; and, when the point vortices are added at the current time step, the vortices of the previous time step should be inserted simultaneously. The interpolations for all variables at the current time step would be a simple way for the point insertion, but this method yields oscillations from errors and results in a failure of the computation. We give the pseudocode of our point insertion method below.

Point insertion algorithm

If $\Delta s_i^{n+1}>\Delta s_{lim}$,

Step 1: Add a new point $\mathbf{x}_p^n$ in the middle of $\mathbf{x}_i^n$ and $\mathbf{x}_{i+1}^n$ by an interpolation.

Step 2: Interpolate γ_p^n and $d\mathbf{U}_p^n/dt$ at the new point $\mathbf{x}_p^n$.

Step 3: Compute the velocity $\mathbf{U}_p^n$ at the new point $\mathbf{x}_p^n$ from Eqs. (12) and (13).

Step 4: Advance the new point to $\mathbf{x}_p^{n+1}$ by a time integration.

Step 5: Interpolate γ_p^{n+1} at the new point $\mathbf{x}_p^{n+1}$.

Step 6: Compute the velocity $\{\mathbf{U}_i^{n+1}\}$ at all marker points from Eqs. (12) and (13).

A schematic for the point insertion procedure is illustrated in Fig. 1. For the interpolations in the algorithm, we use the third-order Lagrange polynomial

$$Q_p=c_{i-1}Q_{i-1}+c_iQ_i+c_{i+1}Q_{i+1}+c_{i+2}Q_{i+2}, \quad (16)$$

$$c_i=\prod_{j\neq i}(s_p-s_j)\Big/\prod_{j\neq i}(s_i-s_j), \quad (17)$$

where s_i is the arclength from $\mathbf{x}_0$ to $\mathbf{x}_i$. We checked that a fifth-order polynomial interpolation gave nearly the same re-

sults for the solution. The segment of the arclength is evaluated by the Euclidean distance

$$\Delta s_i = \sqrt{(x_{i+1} - x_i)^2 + (y_{i+1} - y_i)^2}. \tag{18}$$

For the arclength, a higher-order formula such as the Simpson rule may be applied, but no improvement was found from the result using Eq. (18).

C. Shock-capturing scheme for vortex sheet strength equation

In the computations of Eq. (9), we apply the central difference for $\mathbf{s}$ and $\frac{\partial \mathbf{U}}{\partial s}$. However, the discretization of the term with γ^2 in Eq. (9) should be carefully taken. As time proceeds, the vortex sheet strength develops a complicated structure and becomes very steep around the center of the rollup. This shocklike behavior of vortex sheet strength is due to the term with γ^2, because this term makes Eq. (9) a type of the Burgers equation. Discretizations based on central differences for $\partial\gamma^2/\partial s$ are numerically unstable, and the computations stop when the profile becomes steep.

The similarity of Eq. (9) to the Burgers equation suggests the use of the shock-capturing method for the term $\partial\gamma^2/\partial s$. Previously the first-order Godunov method was applied to the computation of $\partial\gamma^2/\partial s$ [13,17]. The Godunov method approximates the term $F=-\gamma^2$ at the midpoints between vortices by

$$F_{i+1/2} = -\max[(\gamma_i^+)^2, (\gamma_{i+1}^-)^2], \tag{19}$$

where

$$\gamma^+ = \max(-\gamma, 0), \quad \gamma^- = \min(-\gamma, 0). \tag{20}$$

Then $\partial\gamma^2/\partial s$ at $\mathbf{x}_i$ is calculated by $(F_{i+1/2} - F_{i-1/2})/\delta s_i$. Although this formulation based on the Godunov method provides stable computations for Eq. (9), and it runs much longer time than central differences, it is only first-order accurate and thus smoothes the shocks and peaks of the profile. A high-order method is needed for accurate computations, especially in the long-time simulations, but a difficulty is again the nonuniform distribution of the point vortices. As mentioned earlier, most of shock-capturing methods are developed for the uniform grid.

For the high-order computation of the vortex sheet strength, we apply the WENO scheme [19,20]. A general framework for the WENO scheme on the nonuniform grid was established by Shu [19]. Recently an efficient formulation of the fifth-order WENO scheme on the nonuniform grid was presented by Wang *et al.* [20], and we employ this formulation of the WENO scheme for the computation of $\partial\gamma^2/\partial s$. The details of the fifth-order WENO scheme on the nonuniform grid are referred to [20]. Here, we give only a brief description of the WENO scheme, for the vortex method.

The key idea of the essentially nonoscillatory (ENO) scheme is to choose from among several candidates the stencil on which the solution varies the most smoothly and then approximates the flux at the cell boundaries with a high order of accuracy, thus avoiding spurious oscillations caused by interpolating data across discontinuities. The WENO scheme uses a convex combination of all the ENO candidate stencils. Given r ENO stencils of order r, the weights for the WENO scheme are chosen such that the numerical flux is approximated to order $2r-1$ in the smooth region, while in regions near discontinuities the WENO scheme emulates the ENO method.

In the vortex method, the left and right states of the vortex sheet strength at the cell boundaries, denoted by $\gamma_{i+1/2,l}$ and $\gamma_{i+1/2,r}$, are reconstructed by the fifth-order WENO scheme on the nonuniform grid. Then the Godunov flux

$$F_{i+1/2} = -\max[(\gamma_{i+1/2,l}^+)^2, (\gamma_{i+1/2,r}^-)^2] \tag{21}$$

is used for $F=-\gamma^2$ at the cell boundaries.

IV. NUMERICAL RESULTS

To apply the described numerical algorithm to unstable interfaces, the position and the vortex sheet strength of all vortex points should be given initially. We focus on the evolutions of the initial sinusoidal interface of one wavelength,

$$x_i = \frac{i}{N}, \quad y_i = a_0 \sin 2\pi x_i. \tag{22}$$

The initial condition for the vortex sheet strength can be obtained from the linear theory [8]. The initial condition for the local circulation is given by

$$\Gamma_i = \left[1 + 2\pi a_0 \left(A \sin 2\pi x_i - \frac{2\sqrt{r}}{1+r} \cos 2\pi x_i\right)\right] \frac{1}{N}, \tag{23}$$

where r is the density ratio, $r=\rho_1/\rho_2$. The vortex sheet strength is determined from Eq. (14).

All results in this section are plotted in dimensionless units. The dimensionless length and time are given by $\mathbf{x}'=\mathbf{x}/L$ and $t'=t\Delta u/L$, where L is the wavelength of the interface and Δu is the velocity difference across the interface. The vortex sheet strength is also nondimensionalized as $\gamma'=\gamma/(\Delta u L)$. We suppress the primes in the dimensionless variables for shortness.

For long-time simulations, we take two cases of the Atwood number: $A=0.05$ and $A=0.3$. The Atwood number $A=0.05$, corresponding to the density ratio of 1:1.105, represents a weakly stratified case, and $A=0.3$, corresponding to the density ratio of 1:1.857, is chosen for a moderately stratified case. We do not consider a strongly stratified case since for $A \gg 0.5$ the KH instability has a weak rollup [13].

We first examine the performance of the shock-capturing schemes for the vortex sheet strength. Figures 2 and 3 are the comparisons of the results for the interface evolution from the Godunov and WENO schemes for $A=0.05$ and $A=0.3$, respectively. The times are $t=0$, 0.6, 0.8, 1.0, and 1.1 in Figs. 2 and 3. The initial amplitude of the interface is set to $a_0=0.01$, and the regularization parameter is $\delta=0.1$; these values are used in all our computations. The number of point vortices is fixed to $N=400$. Figures 2 and 3 show that the results of the Godunov scheme are overlapped to the WENO scheme for both $A=0.05$ and $A=0.3$. More rollups are found for the smaller density jump, which is a well-known behavior in the KH instability, and the vortex core is more moved to the left for the larger density ratio.

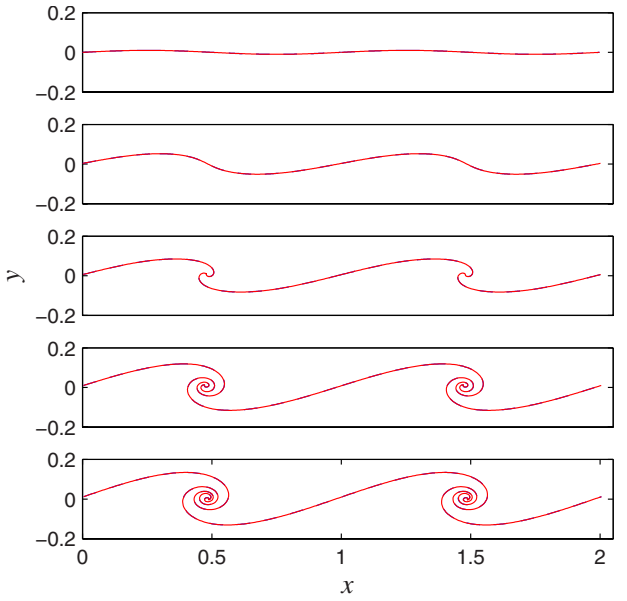

FIG. 2. (Color online) Comparison of the interface evolution from the Godunov and WENO schemes for $A=0.05$. The times are $t=0$, 0.6, 0.8, 1.0, and 1.1. The solid curves correspond to the WENO scheme and the dashed curves correspond to the Godunov scheme.

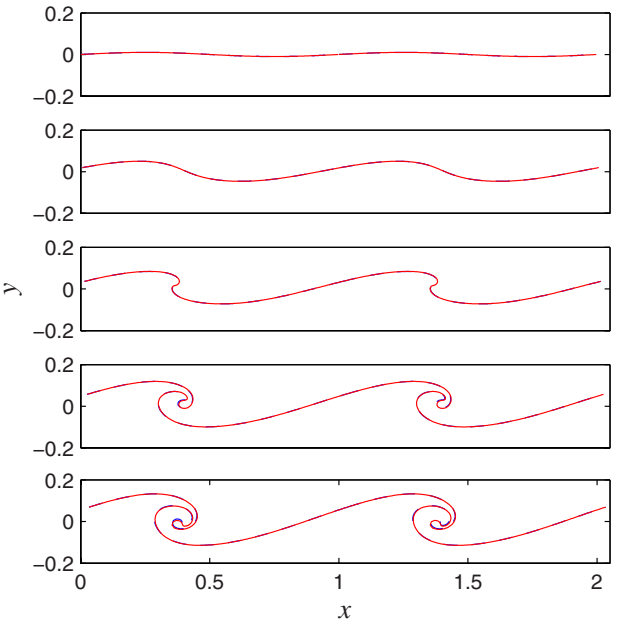

FIG. 3. (Color online) Comparison of the interface evolution from the Godunov and WENO schemes for $A=0.3$. The times are $t=0$, 0.6, 0.8, 1.0, and 1.1. The solid curves correspond to the WENO scheme and the dashed curves correspond to the Godunov scheme.

Figure 4 is the comparison of the vortex sheet strength for Figs. 2 and 3 at selected times. The x axis is the normalized arclength, which is scaled by the total arclength. We see that the results from the WENO scheme are sharper and higher around the peak than those from the Godunov scheme, and the differences of the results between the Godunov and WENO schemes are larger at the later time.

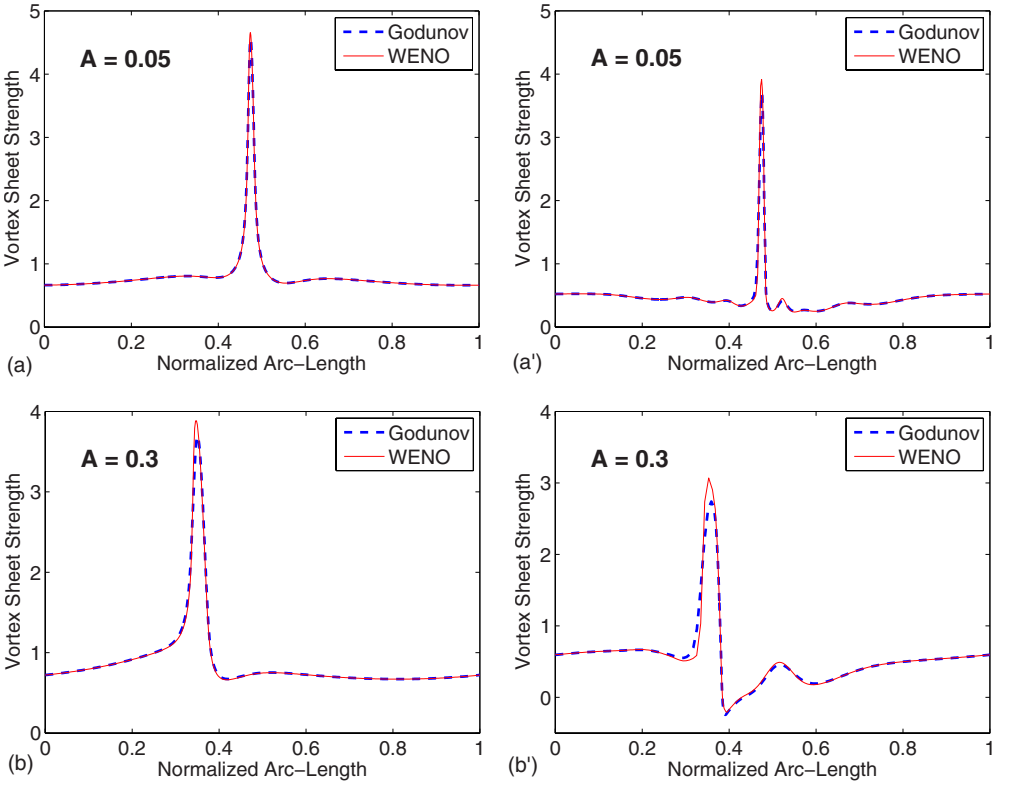

FIG. 4. (Color online) Comparisons of the vortex sheet strength for $A=0.05$ and $A=0.3$ at selected times. (a) $A=0.05$, $t=0.8$; (a′) $A=0.05$, $t=1.1$; (b) $A=0.3$, $t=0.8$; and (b′) $A=0.3$, $t=1.1$.

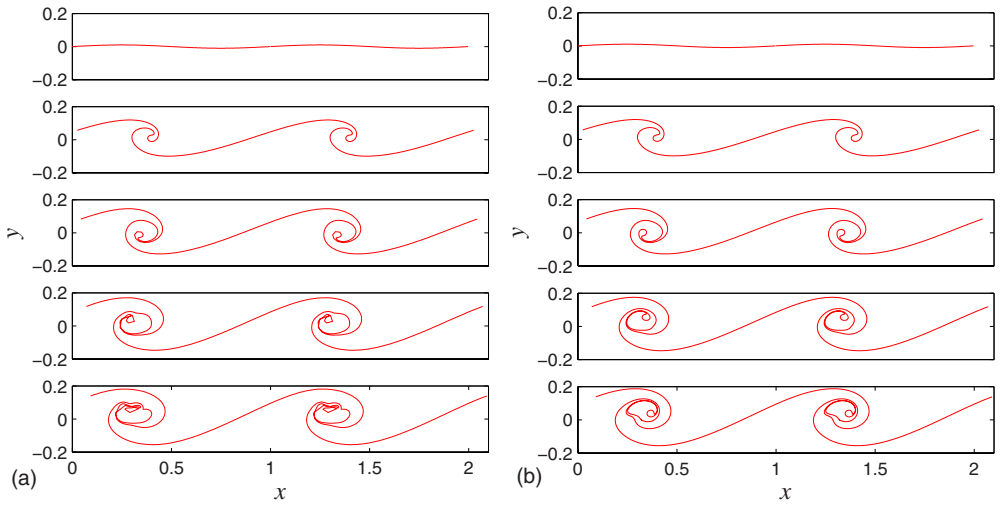

FIG. 5. (Color online) Comparison of the results without and with the point insertion for $A=0.3$. The times are $t=0$, 1, 1.2, 1.4, and 1.5. (a) Point insertion not used and (b) point insertion used.

Figure 5 is the comparison of the results from the WENO scheme without and with the point insertion for $A=0.3$. Figure 5(a) is the result with the fixed number of points $N=400$, and Fig. 5(b) is the result with the point insertion, initially starting with $N=400$. The arclength limit for the point insertion is set to $\Delta s_{lim}=0.003$, and this value is used in all our computations. In Fig. 5(a), we find that the result without the point insertion lacks the resolution around the vortex core at $t=1.4$ and is poorly resolved at $t=1.5$. Figure 5(b) shows that the interface is well resolved by the point insertion. Note that the number of points at $t=1.5$ in Fig. 5(b) is $N=1686$.

Figure 6 is the comparison of the results from the Godunov scheme with $N=1600$ and the WENO scheme with the point insertion, for $A=0.3$ at $t=1.0$. The number of points for the WENO scheme with the point insertion at $t=1.0$ is $N=817$, which is much fewer than $N=1600$. Figure 6(a) is the result for the interface, and Fig. 6(b) is the result for the vortex sheet strength with respect to the normalized arclength. We see in Fig. 6 that the WENO scheme with the point insertion gives the same result for the interface profile as the Godunov scheme with $N=1600$, and is even better for the vortex sheet strength. Figure 6 validates the accuracy and efficiency of our point insertion method and the WENO scheme.

Figures 7 and 8 are the long-time evolutions of the interface, using the point insertion, for $A=0.05$ and $A=0.3$, respectively. The times are $t=0$, 1.1, 1.5, 1.8, and 2.2. Figures 7 and 8 show that our numerical method using the point insertion successfully simulates the KH instability at late times. For $A=0.05$, the interface rolls up uniformly in a large scale. For $A=0.3$, the interface evolves a secondary instability at $t=1.5$, where the inside of the rollup is distorted, and eventually develops to a complex shape. It will be discussed shortly that the secondary instability would be caused by the occurrence of new peaks and shocks on the vorticity. Note that the distortion of the internal rollup was also reported in a recent paper on the high-order computation of the Richtmyer-Meshkov instability [22], which is a shock-induced interfacial instability. The rollup in the Richtmyer-Meshkov instability is a type of the KH instability. In Figs. 7 and 8, we also observe that the vortex cores keep moving to the left, shifting faster for the larger density ratio. For

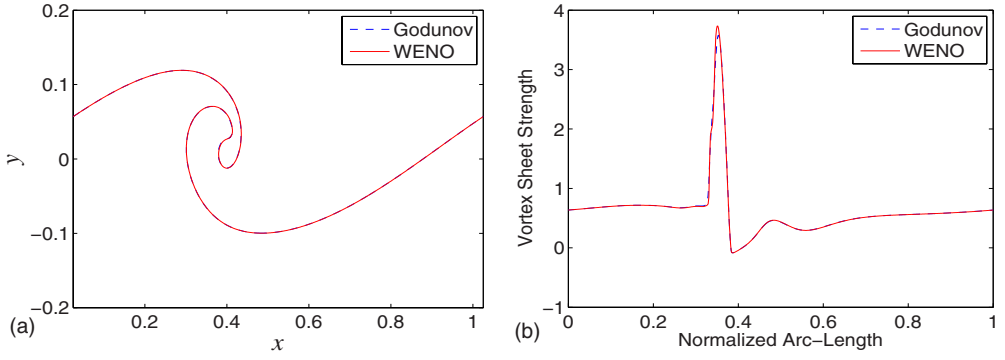

FIG. 6. (Color online) Comparison of the results from the Godunov scheme with $N=1600$ and the WENO scheme with the point insertion, for $A=0.3$ at $t=1.0$. The number of points for the WENO scheme at $t=1.0$ is $N=817$. (a) Interface and (b) vortex sheet strength vs normalized arclength.

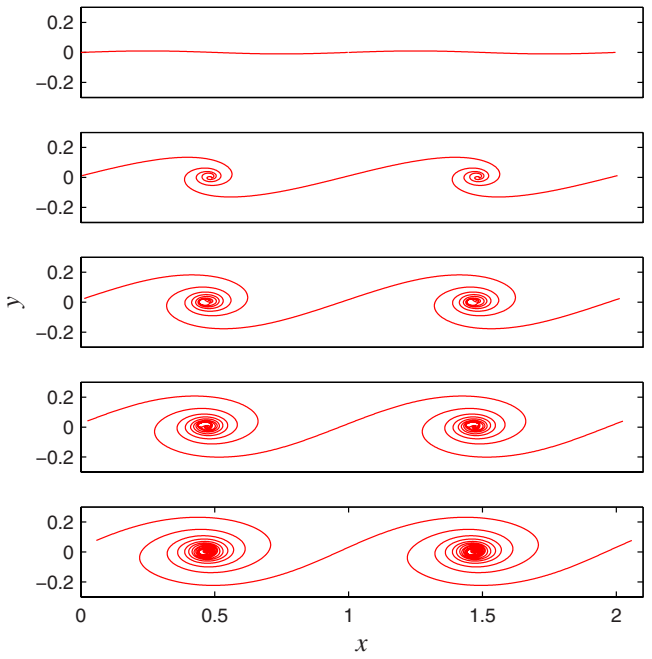

FIG. 7. (Color online) Long-time evolution of the interface for $A=0.05$. The times are $t=0$, 1.1, 1.5, 1.8, and 2.2.

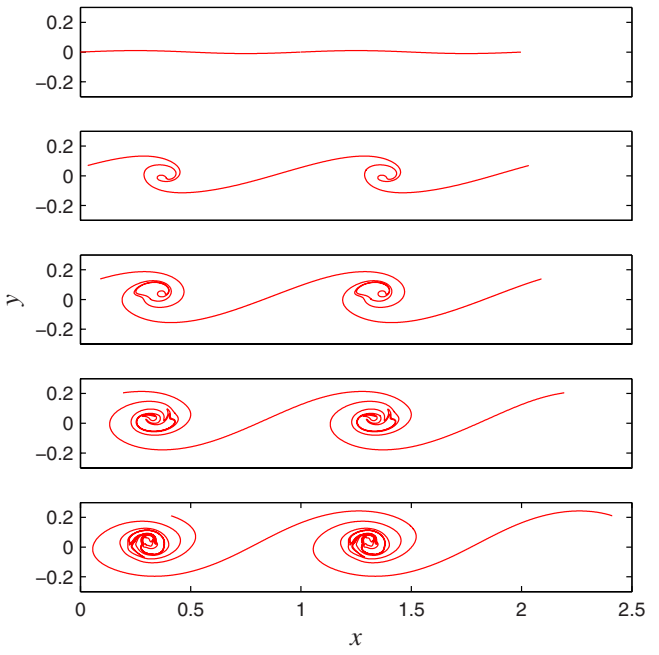

FIG. 8. (Color online) Long-time evolution of the interface for $A=0.3$. The times are $t=0$, 1.1, 1.5, 1.8, and 2.2.

$A=0.3$, the left end point moves to the right, over the vortex core.

Figure 9 is the zooming of the interface for $A=0.05$ around the vortex core in Fig. 7 at $t=1.8$ and 2.2. The locations of point vortices are also given in Figs. 9(a′) and 9(b′). Figure 9 shows that the vortex core is well resolved by the point insertion method. We find that the rollup in the vortex center is not uniform and the secondary instability also occurs for $A=0.05$ in a small scale. The interface for $A=0.05$ at $t=2.2$ maintains a relatively uniform shape, compared to that for $A=0.3$ at the same time, shown in Figure 10. Figure 10 is the zooming of the interface for $A=0.3$ in Fig. 8 around the vortex core at $t=1.8$ and 2.2. Only the locations of point vortices are given in Fig. 10. We clearly see the core structure for $A=0.3$ in the fine resolution. The secondary instability is pronounced at $t=1.8$, and the interface forms a complex disordered internal structure at $t=2.2$. We examined that the small-scale instability always occurred for varying Δs_{lim} or the regularization parameter δ. Similar results were ob-

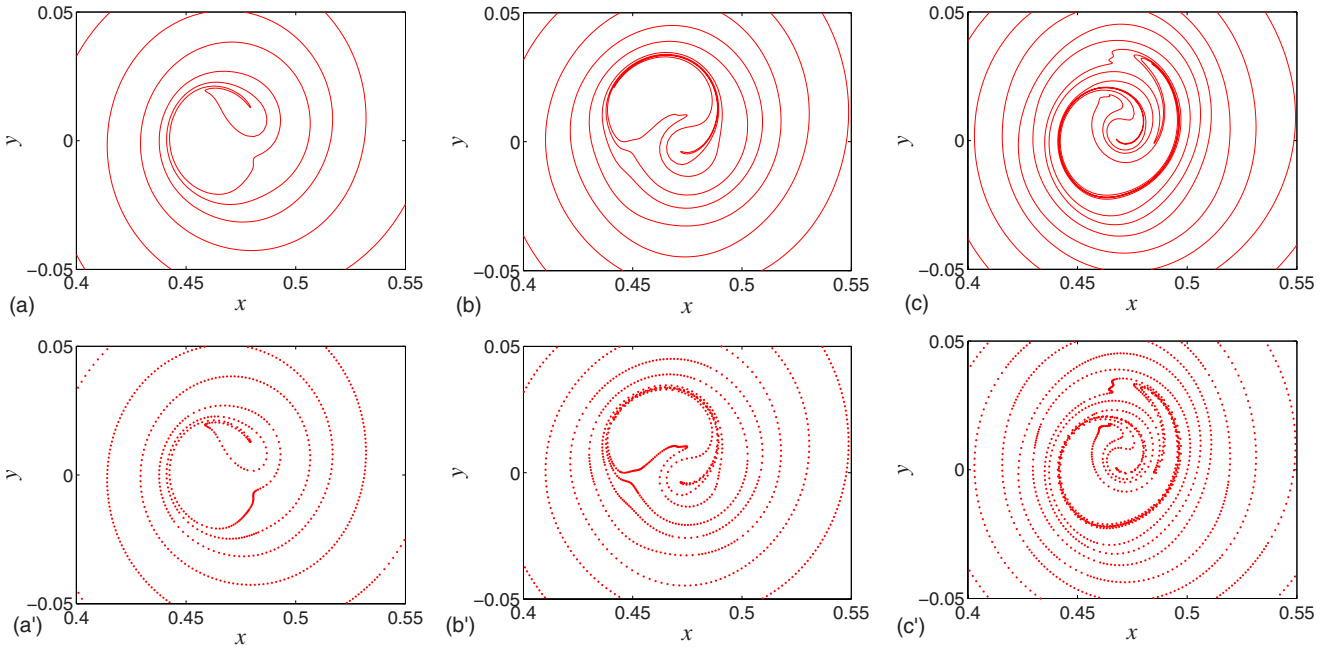

FIG. 9. (Color online) Zooming of the interface for $A=0.05$. (a), (b), and (c) correspond to the solutions at $t=1.5$, 1.8, and 2.2 in Fig. 7, respectively. (a′), (b′), and (c′) are the locations of vortices for (a), (b), and (c).

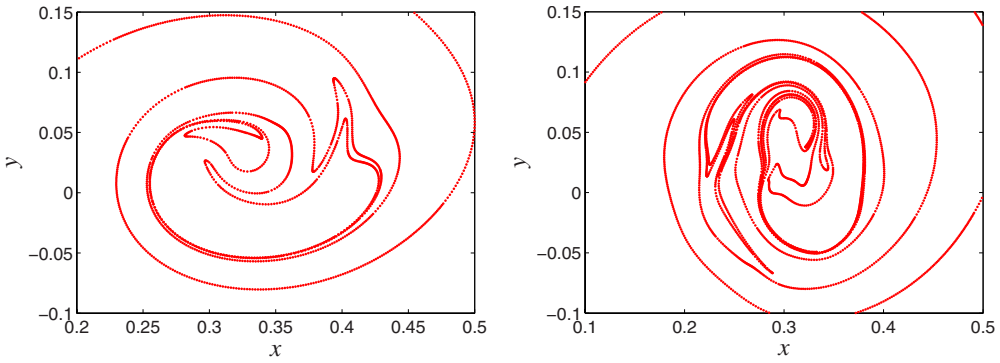

FIG. 10. (Color online) Zooming of the interface for $A=0.3$. The left and right plots correspond to the solutions at $t=1.8$ and 2.2 in Fig. 8, respectively.

tained for smaller values of Δs_{lim}. For a larger value of δ, the sheet rolls up slower and the small-scale features appear later.

Krasny and Nitsche [23] showed that in the uniform fluid, irregular small-scale features developed at late times: gaps and folds appeared in the spiral core. They attributed the irregular features to the onset of chaos in the vortex sheet. In the stratified fluids, the vortex sheet has a small-scale instability at late times, but the gaps in the spiral are not found. The gaps in the uniform fluid were occurred from a resonance after a number of rollups. However, in the stratified fluids, the secondary instability breaks a uniform rollup in the inner core, and thus a resonance may not arise. Figure 9 shows that the neck of the rollup is dragged into the core, and then the fold appears, which may be a different mechanism from the resonance. The relation of the secondary instability to chaos is uncertain and would be an interesting subject for further study.

Figure 11 is the growth of the arclength of the interface and the number of points scaled by the initial number of points, $N(t)/N(t=0)$, for $A=0.3$. Figure 11 shows that the arclength of the interface grows exponentially, and the number of points increases with a similar rate as the arclength of the interface.

Figure 12 is the vortex sheet strength along the interface for Figs. 7 and 8, at $t=1.5$ and 2.2. For $A=0.05$, the peaks of the vortex sheet strength are distinguished and concentrated near the center, but for $A=0.3$, many peaks and shocks are evolved at $t=2.2$ and spread over the interface. Compared to Fig. 4, new peaks and shocks of the vortex sheet strength are found at $t=1.5$ for both $A=0.05$ and $A=0.3$. In Figs. 7 and 8, the secondary instability on the inside of the rollup is observed at $t=1.5$. Thus, the new peaks and shocks of the vortex sheet strength may yield the secondary instability on the interface, and eventually the complex structure of the vortex sheet strength leads to the disordered profile of the interface. We also find that for both cases, the highest peak of the vortex sheet strength at $t=2.2$ is slightly decreased than that at $t=1.5$. This behavior of the decrease in the peak of the vortex sheet strength is also found in Fig. 4 for both $A=0.05$ and 0.3, comparing at $t=0.8$ and 1.1. Therefore, we may conclude that in the KH instability, the vortex sheet strength apparently becomes singular and has a single peak at an early time, and then after reaching a possible maximum, this peak is reduced and other peaks and shocks are formed over the interface, and at a late time the vortex sheet strength is developed to a chaotic structure.

Figure 13 is the curvature along the interface for $A=0.05$ and $A=0.3$, at $t=1.5$ and 2.0. Figure 13 shows that for both cases of $A=0.05$ and $A=0.3$, the curvature is very singular around the vortex core, but for $A=0.3$ the singularities of the curvature are more spread over the interface, similarly as the vortex sheet strength.

Figure 14 is the vorticity field for $A=0.05$ and $A=0.3$, at $t=2.2$. The vorticity ω is defined as $\nabla\times\mathbf{U}=\omega\mathbf{k}$, where $\mathbf{k}$ is the unit vector in the z axis. In Fig. 14, the vorticity is reconstructed from the regularized velocity field, computed on a rectangular grid. The velocity field is obtained from Eqs. (10) and (11), taking x and y in the fluid region. We see in Fig. 14 that for $A=0.05$ the vorticity is uniformly concentrated on the center of the rollup and is almost symmetric. For $A=0.3$ the vorticity has two cores, one strong and another mild, and the intensity of the vorticity on the cores is weaker than that for $A=0.05$. We also find an interesting behavior for $A=0.3$ that the upper arm of the rollup, winding clockwise, has a relatively strong vorticity, comparable to that in the inside of the rollup, while the vorticity of the lower arm, winding counterclockwise, is weak.

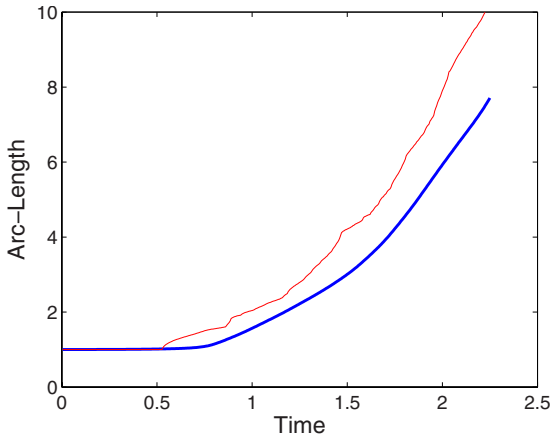

FIG. 11. (Color online) Growth of the arclength of the interface and the number of points, scaled by the initial number of points, for $A=0.3$. The thick curve is the total arclength and the thin one is $N(t)/N(t=0)$.

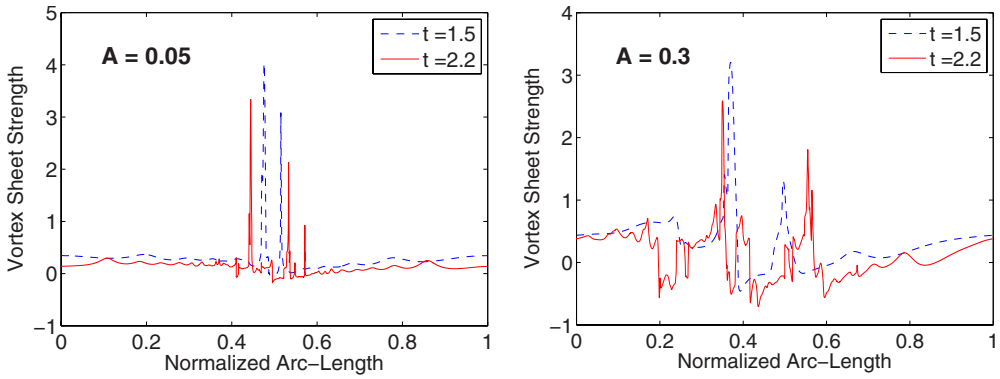

FIG. 12. (Color online) Vortex sheet strength along the interface for $A=0.05$ and 0.3.

V. CONCLUSIONS

We have presented the long-time computations for the KH instability in density-stratified fluids by the adaptive vortex method. The numerical results show that our vortex method successfully simulates the chaotically distorted interfaces of the KH instability at late times.

We have applied the point insertion procedure and the high-order shock-capturing method to the vortex method. The point insertion procedure provides the fine resolution for the interface at late times, and the numerical results validate the accuracy and robustness of our point insertion method. The high-order shock-capturing method, based on the fifth-order WENO scheme on the nonuniform grid, for the computation of the vortex sheet strength enhances the accuracy of the vortex method around the peaks and shocks. The point insertion procedure and the high-order shock-capturing method greatly improve the capability and the applicability of the vortex method.

The various aspects of late-time dynamics of the KH instability have been investigated by the vortex method. It is found that the KH instability evolves the secondary instability at a late time and eventually develops to a disordered structure. For a weakly stratified case, the interface has a uniform rollup in a large scale except the vortex center, and the vorticity is concentrated on the core. For a moderately stratified case, the vorticity is spread from the center of the rollup, the secondary instability is pronounced, and the interface forms a complex internal structure.

It has been known that the KH instability induces a mixing of stratified fluids through a transition from two-dimensional laminar flows to a three-dimensional turbulence

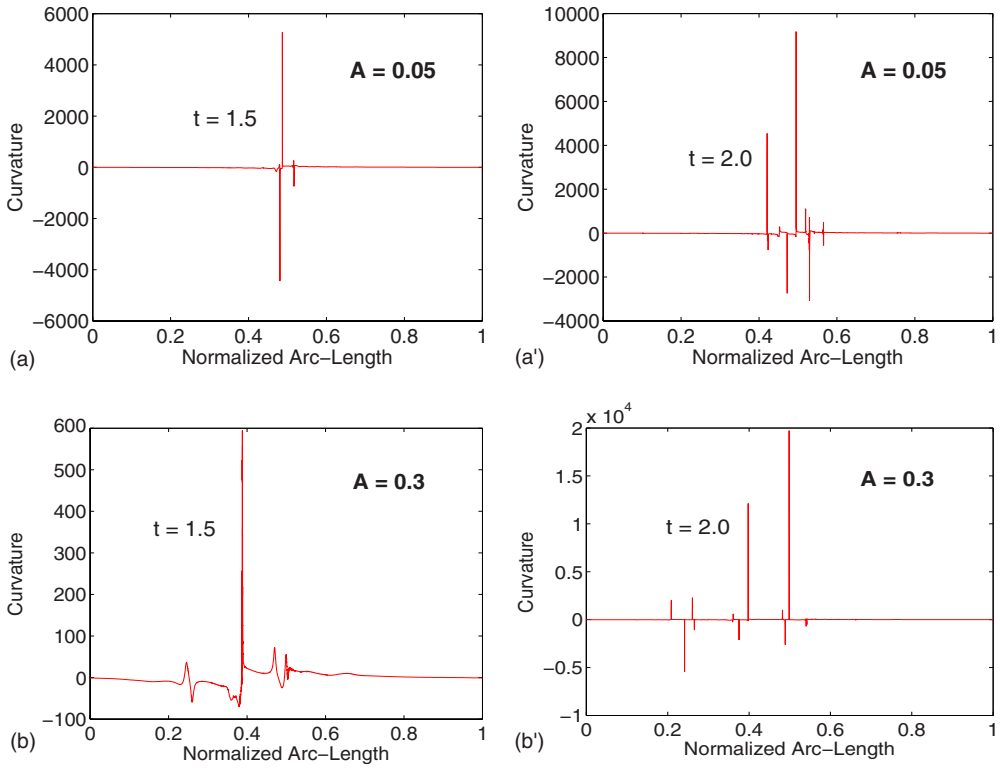

FIG. 13. (Color online) Curvature along the interface for $A=0.05$ and $A=0.3$. (a) $A=0.05$, $t=1.5$; (a′) $A=0.05$, $t=2.0$; (b) $A=0.3$, $t=1.5$; and (b′) $A=0.3$, $t=2.0$.

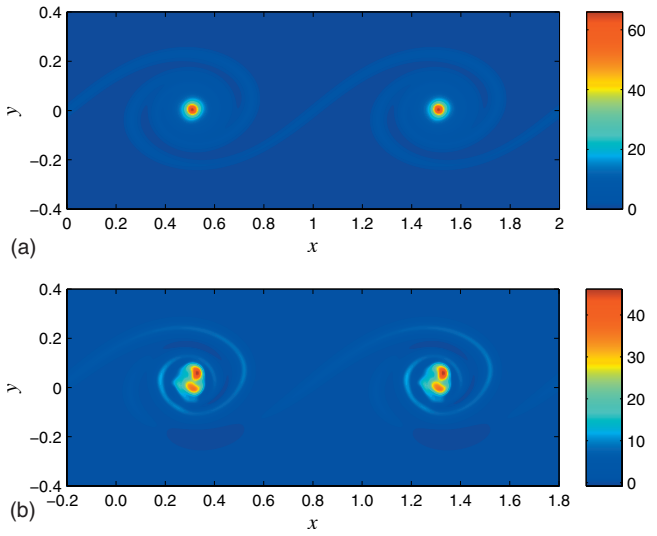

FIG. 14. (Color) Vorticity field at $t=2.2$. The vorticity is reconstructed from the regularized velocity field. (a) $A=0.05$ and (b) $A=0.3$.

[4]. Several authors identified the transition to turbulence of a mixing layer with the onset of three-dimensional irregular small-scale motions in the core of the two-dimensional KH wave [4,24,25]. This suggests that the secondary instability on the core of the rollup may cause the transition to turbulence, and may develop to a three-dimensional motion at a later time. For a complete modeling of late-time motions of the KH instability, three-dimensional simulations would be necessary.

It was shown by Tryggvason *et al.* [9] that in the uniform fluid, the regularized vortex model for inviscid fluids reproduced many of features associated with the viscous flows with increasing Reynolds number, but it gave more rollups in the core than the results for the viscous flows. We thus surmise that the late-time complex motions from our simulations would not be exactly same as the *real flows* (viscous flows). Nevertheless, our simulations show main features of the late-time dynamics of the KH instability in stratified fluids, and illustrate the instability mechanism on the core of the interface, for the transition to turbulence.

ACKNOWLEDGMENTS

We thank Sun-Chul Kim for helpful discussions. We also would like to thank anonymous referees for valuable comments and suggestions. This research was supported by Basic Science Research Program through the National Research Foundation of Korea (NRF) funded by the Ministry of Education, Science and Technology (Grants No. 2010-0012152 and No. 2010-0025523).

[1] G. Birkhoff, *Proceedings of Symposia in Applied Mathematics* (American Mathematical Society, Providence, 1962), Vol. XIII, p. 55.
[2] S. Chandrasekhar, *Hydrodynamic and Hydromagnetic Stability* (Oxford University Press, Oxford, 1962).
[3] M. Lesieur, *Turbulence in Fluids* (Kluwer Academic, Dordrecht, 1990).
[4] W. R. Peltier and C. R. Caulfield, Annu. Rev. Fluid Mech. **35**, 135 (2003).
[5] G. R. Baker, D. I. Meiron, and S. A. Orszag, Phys. Fluids **23**, 1485 (1980).
[6] D. W. Moore, Proc. R. Soc. London, Ser. A **365**, 105 (1979).
[7] R. Krasny, J. Comput. Phys. **65**, 292 (1986).
[8] R. H. Rangel and W. A. Sirignano, Phys. Fluids **31**, 1845 (1988).
[9] G. Tryggvason, W. J. A. Dahm, and D. Sbeih, ASME Trans. J. Fluids Eng. **113**, 31 (1991).
[10] T. Y. Hou, J. S. Lowengrub, and M. J. Shelley, Phys. Fluids **9**, 1933 (1997).
[11] T. Sakajo and H. Okamoto, J. Phys. Soc. Jpn. **67**, 462 (1998).
[12] S.-C. Kim, J.-Y. Lee, and S.-I. Sohn, J. Phys. Soc. Jpn. **72**, 1968 (2003).
[13] S.-I. Sohn and W. Hwang, J. Phys. Soc. Jpn. **74**, 1472 (2005).
[14] R. Krasny, J. Fluid Mech. **184**, 123 (1987).
[15] R. M. Kerr, J. Comput. Phys. **76**, 48 (1988).
[16] R. J. LeVeque, *Numerical Methods for Conservation Laws* (Birkhäuser, Basel, 1992).
[17] J. A. Zufiria, Phys. Fluids **31**, 3199 (1988).
[18] X. D. Liu, S. Osher, and T. Chan, J. Comput. Phys. **115**, 200 (1994).
[19] C.-W. Shu, *Advanced Numerical Approximation of Nonlinear Hyperbolic Equations*, Lecture Notes in Mathematics Vol. 1697 (Springer-Verlag, Berlin, 1998), p. 325.
[20] R. Wang, H. Feng, and R. J. Spiteri, Appl. Math. Comput. **196**, 433 (2008).
[21] G. Tryggvason, J. Comput. Phys. **80**, 1 (1989).
[22] M. Latini, O. Schilling, and W. S. Don, Phys. Fluids **19**, 024104 (2007).
[23] R. Krasny and M. Nitsche, J. Fluid Mech. **454**, 47 (2002).
[24] S. A. Thorpe, J. Fluid Mech. **61**, 731 (1973).
[25] L. P. Bernal and A. Roshko, J. Fluid Mech. **170**, 499 (1986).